Shear-layer structures in turbulence generated by opposed multiple-fan arrays

Zexu Han[a], Haruyuki Sakai[a], Tomoaki Watanabe[a,*] and Koji Nagata[a]

[a]*Department of Mechanical Engineering and Science, Kyoto University, Kyoto, 615-8540, Japan*

ARTICLE INFO

Keywords:
Turbulent structures
Triple decomposition
Shear layers

ABSTRACT

Shear layers arising from turbulent velocity fluctuations are important flow structures that strongly influence heat and mass transfer, but their characteristics have been examined in only a limited range of flows. The present study investigates shear layers in turbulence generated by opposed multiple-fan arrays. Velocity fields are measured by particle image velocimetry in a multi-fan turbulence chamber under three fan-speed conditions, including nearly isotropic and anisotropic cases. Shear layers are analyzed using the triple decomposition applied to low-pass-filtered velocity fields to examine their scale dependence over the filter range from 20η to 80η, where η is the Kolmogorov scale. The results show that intense shearing motions form layer-like structures. Conditional averaging in a shear-aligned coordinate system reveals that the conditionally averaged shear-vorticity profile is self-similar for filter scales above 30η. The aspect ratio of shear layers remains approximately 4–5 and varies little with scale or flow condition. The mean velocity jump across a shear layer increases with scale and is reasonably scaled by $(\varepsilon\delta_S)^{1/3}$, where ε is the turbulent kinetic energy dissipation rate and δ_S is the shear-layer thickness, indicating consistency with Kolmogorov scaling. Although the most anisotropic case exhibits larger velocity fluctuations in the fan-axial direction than those in the vertical direction, the probability density function of shear-layer orientation is nearly uniform, and both the aspect ratio and the normalized velocity jump depend only weakly on orientation. These results suggest that the fundamental characteristics of shear layers at scales of $O(10^1\eta)$ are robust against large-scale anisotropy.

1. Introduction

Turbulent flows efficiently transfer heat and mass through chaotic fluid motions over a wide range of scales. This enhanced transport plays an essential role in many natural and engineering flows. In the atmosphere and oceans, turbulence governs the dispersion of heat, moisture, salinity, and chemical species, thereby influencing weather, climate, and environmental transport [1, 2, 3, 4]. In engineering applications, turbulent mixing determines the performance of heat exchangers, combustion devices, chemical reactors, and ventilation systems, where rapid transport of momentum, heat, and scalar quantities is often required [5, 6, 7, 8]. Because of its strong impact on transport efficiency, turbulence has long been a central subject in fluid mechanics and heat and mass transfer.

One important aspect of turbulence is its structure, which can be perceived as characteristic patterns in flow visualization. Analysis from a flow-structure perspective allows intuitive physical observations [9]. Because turbulence comprises vortical motions at different scales, structures associated with vorticity have been of great interest in understanding turbulent flows from the flow-structure perspective. A velocity gradient tensor $\partial u_i/\partial x_j$ can be

*Corresponding author
watanabe.tomoaki.8x@kyoto-u.ac.jp (T. Watanabe)
ORCID(s): 0000-0002-9375-0075 (T. Watanabe); 0000-0002-8519-5454 (K. Nagata)
 The published version is available at https://doi.org/10.1016/j.icheatmasstransfer.2026.112209.

decomposed into symmetric and antisymmetric components, which are called the rate-of-strain tensor $S_{ij} = (\partial u_i/\partial x_j + \partial u_j/\partial x_i)/2$ and the rate-of-rotation tensor $\Omega_{ij} = (\partial u_i/\partial x_j - \partial u_j/\partial x_i)/2$. The component of Ω_{ij} is proportional to the vorticity vector component $\omega_i = \epsilon_{ijk}\partial u_k/\partial x_j$, where ϵ_{ijk} is the Levi-Civita symbol. Additionally, Ω_{ij} can be further decomposed into two components associated with rigid-body rotation and shear [10]. These two distinct motions manifest as vortex tubes with rigid-body rotation and vortex sheets with shear. The former is often identified in flows based on the second invariant of the velocity gradient tensor, $Q = (\Omega_{ij}\Omega_{ij} - S_{ij}S_{ij})/2$, whose positive values indicate that rotation predominates over strain [11]. An alternative method for identifying vortex tubes is the λ_2 criterion [12]. These identification methods have led to extensive studies of vortex tubes in various turbulent flows [13, 14, 15, 16, 17, 18, 19, 20]. Statistical analyses of vortex tubes with respect to the radial position from the vortex center have revealed their characteristics, such as diameter and azimuthal velocity.

Compared with vortex tubes, vortex sheets associated with shear, also called shear layers, were investigated less extensively in early studies of vortical structures, except through observations based on flow visualization [21]. Visualization of vorticity in three-dimensional space reveals intense vorticity concentrated in layers, whose evolution suggests that vortex tubes are generated by the instability of shear layers. A more recent method for identifying shear layers is based on the triple decomposition of the velocity gradient tensor [10]. This decomposition splits the velocity gradient into three parts: elongation, rigid-body rotation, and shear. The shear component yields the shear-vorticity vector, which is useful for identifying shear layers. Shear layers have been analyzed using the triple decomposition in isotropic turbulence, jets, and mixing layers [22, 23, 24, 25]. These studies have consistently confirmed that small-scale shear layers have characteristic velocity and length scales determined by the Kolmogorov velocity and length scales. It has been shown that small-scale shear layers form within a biaxial strain that stretches the shear-vorticity and sustains the thin-layer structure, exhibiting similarity to Burgers' vortex layer [22]. The triple decomposition applied to a low-pass-filtered velocity gradient tensor extracts the three motions at the filter cutoff scale. Analyses of shear layers in filtered velocity fields have shown that self-similar shear layers exist over a wide range of scales [26]. Recent analyses based on velocity-gradient partitioning have also emphasized the importance of distinguishing pure shearing, rigid-body rotation and normal straining in turbulent velocity-gradient dynamics [27, 28]. In particular, a normality-based analysis of filtered velocity gradients showed that shear layers contribute significantly to inertial- and subinertial-range dynamics [28].

Shear layers play an important role in heat and mass transfer in turbulence. The velocity field induced by small-scale shear layers can be calculated using the Biot-Savart law applied to the shear-vorticity vector. Turbulent jets rapidly transport scalar quantities and momentum in the transverse direction, causing the jet region to expand outward [29, 30, 31, 32, 33]. The shear-induced velocity field has been shown to contribute predominantly to turbulent heat flux in turbulent jets [34]. In contrast, the velocity field reconstructed from the vorticity vector of rigid-body rotation, associated with vortex tubes, has virtually no contribution to the turbulent flux. Additionally, instability of small-scale shear layers has been shown to promote mixing at small scales [35]. These studies have consistently confirmed the importance of shear layers in turbulent transport phenomena. However, investigations of shear layers have been reported for fewer canonical turbulent flows than those of vortex tubes. Vortex tubes are sensitive to variations in large-scale characteristics, such as mean shear, which leads to their preferential alignment with the mean shear direction [36, 37, 38]. The present study therefore examines whether the characteristic geometry, scaling, and orientation statistics of shear layers persist in turbulence with imposed large-scale anisotropy generated by opposed multiple-fan arrays.

The present study investigates shear layers using a turbulence chamber with opposed multiple-fan arrays [39]. The multi-fan turbulence chamber consists of two sets of 9×9 fans placed on opposing sides of a rectangular chamber. Similar fan-driven turbulence chambers have been developed in previous studies [40, 41, 42, 43, 44]. These studies have shown that interactions among fan-induced flows lead to the formation of nearly homogeneous isotropic turbulence with a small mean velocity near the chamber center. The present facility can employ different rotational speeds for each fan row, thereby varying the velocity of fan-induced flows in the vertical direction. When the rotational speed is fixed for all fans, nearly homogeneous isotropic turbulence with a small mean velocity forms near the chamber center [39]. Additionally, large-scale anisotropy can be introduced into the flow by adopting different rotational-speed profiles. The characteristics of shear layers are investigated for turbulence under both isotropic and anisotropic conditions. Velocity measurements are conducted using two-dimensional two-component particle image velocimetry (PIV).

The paper is organized as follows. Section 2 describes the turbulence chamber, experimental conditions, and measurement methods. Section 3 presents the methods adopted to analyze shear layers using velocity data measured by PIV. Section 4 presents the experimental results, including both the fundamental flow characteristics and the characteristics of shear layers. Finally, the main findings are summarized in Sec. 5.

2. Experimental setup and methods

2.1. The multi-fan turbulence chamber

Figures 1(a) and (b) show a schematic of the multi-fan turbulence chamber. The same facility was used in our previous study [39]. The details were presented there, and this section briefly describes the facility and measurement methods. Two multiple-fan arrays are arranged on opposite sides inside a rectangular chamber. The laboratory coordinate system is defined with the origin at the chamber center. The fan-axis and vertical directions are denoted by x and y, respectively, while z is defined as the spanwise direction normal to the x and y directions. Each multiple-fan array comprises 81 DC fans (Sanyo Denki, 9GA0412P3K011), arranged in a 9×9 square configuration with a center-to-center pitch of $p = 60$ mm, as illustrated in Fig. 1(c). The chamber is constructed with an aluminum frame, with

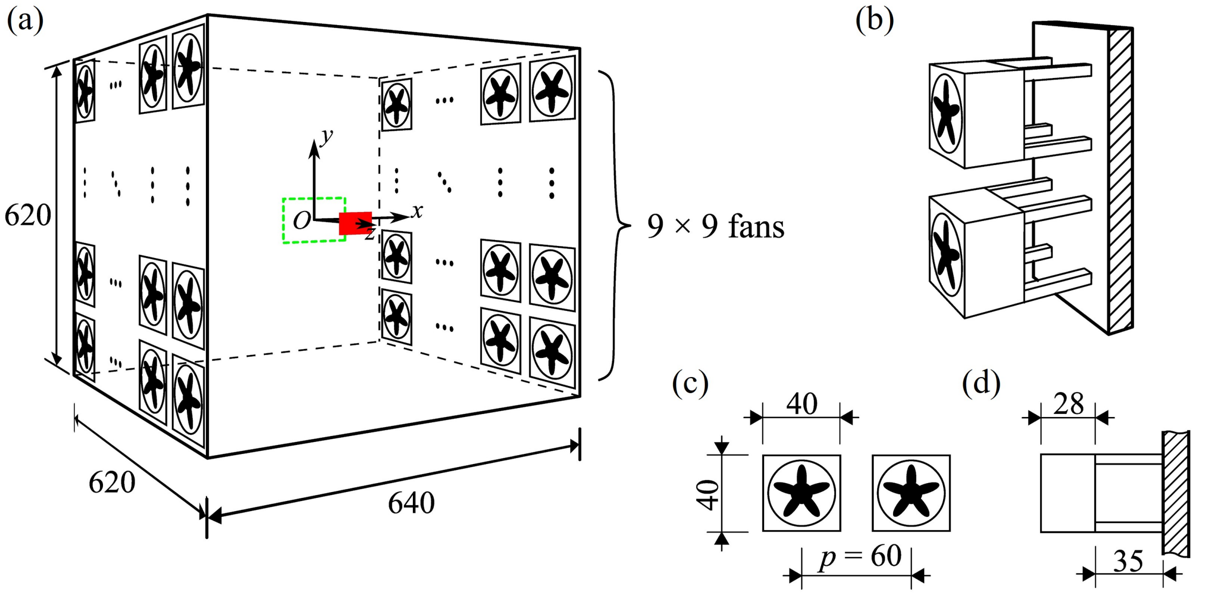

Figure 1: Schematic of the multi-fan turbulence chamber. (a) Overall perspective view of the confined chamber. The fans are illustrated with enlarged dimensions and are not drawn to scale, while installation details are omitted for clarity. The green dashed rectangular frame and the red solid rectangle indicate the large and small FOVs of the PIV measurements, respectively. (b) Perspective view of the installation of two adjacent fans. (c) Front view of two adjacent fans, defining the fan pitch p. (d) Side view of the installation of a fan. The fan blades are shown for schematic purposes only and do not imply any information about their actual geometry or dimensions. All dimensions are in mm.

aluminum plates forming the bases of the fan arrays and clear acrylic panels used for the remaining walls. The internal dimensions of the chamber are $620\times620\times640$ mm^3. Each fan, with dimensions of $40\times40\times28$ mm, is mounted on the aluminum plate with an offset distance of 35 mm using a 3D-printed stand illustrated in Fig. 1(d). These arrangements lead to a distance of 514 mm between the opposed fans. The top wall of the chamber is removable for maintenance and the introduction of tracer particles.

Within each array, each fan row at the same height (y) is connected to a common pulse-width modulation (PWM) controller, which controls the fan rotational speed through a variable duty ratio (DR). The PWM signal has a fixed frequency of 25 kHz. The minimum speed is 6500 rpm at DR = 0%, from which the speed increases with DR. The fan speed is about 8600 rpm at DR = 6%, and then increases linearly with DR to 22000 rpm at DR = 95%, above which it remains constant. The flow rate is 1.35×10^{-2} m^3/s at DR = 100% and 0.38×10^{-2} m^3/s at DR = 0%.

2.2. Experimental conditions

Different DR settings lead to turbulence with different properties. Experiments are conducted for the three cases summarized in Table 1. Here, the fan rows are indexed from bottom to top along the y direction, with n_f = 1–9. Array number distinguishes the two arrays to present the DR settings for each array, although the arrays are identical. Case 1

Case	DR for array 1 (%)	DR for array 2 (%)
1	100 for all n_f	100 for all n_f
2	$10 + 10 \times n_f$	$110 - 10 \times n_f$
3	$\begin{cases} 100 & \text{for } 5 \le n_f \le 9 \\ 0 & \text{otherwise} \end{cases}$	$\begin{cases} 100 & \text{for } 1 \le n_f \le 5 \\ 0 & \text{otherwise} \end{cases}$

Table 1
DR settings for each case. Here, n_f = 1–9 is the index distinguishing the fan rows

applies the same DR to all fans. This setting was used in our previous study to produce nearly homogeneous isotropic turbulence near the chamber center [39]. In Case 2, DR varies linearly from 10 to 100. For array 1, DR increases from bottom to top, while the profile is reversed for array 2. Case 3 applies DR = 100 or 0. Cases 2 and 3 are intended to introduce anisotropy into the flow, with mean shear near the fans.

2.3. Velocity measurement

Two-dimensional, two-component PIV is employed to measure velocity vectors in the x and y directions, (U, V), on x–y planes near the chamber center. The PIV system consists of a double-pulse Nd:YAG laser (Dantec Dynamics, Dual Power 65-15) and a high-speed camera (Dantec Dynamics, SpeedSense 9070) with a resolution of 1280×800 pixels, operated using integrated software (Dantec Dynamics, DynamicStudio) with a synchronizer (Dantec Dynamics, 80N77). Tracer particles, with a mean diameter of approximately 1 μm, are generated using a fog generator (Dantec Dynamics, SAFEX F2004) and a fog fluid (Dantec Dynamics, Fog Fluid Standard). The particles are seeded into the chamber prior to each measurement. The laser illuminates the measurement plane from bottom to top, and the camera is aligned along the z axis. The particle image pairs are acquired at a sampling rate of 15 Hz and processed using the adaptive PIV algorithm [45] together with the universal outlier detection method [46] for erroneous vector handling, both of which are implemented in DynamicStudio. The particle image pairs are processed with a prescribed vector spacing of 8 pixels, with a minimum interrogation window size of 16×16 pixels (corresponding to a 50% overlap) and a maximum window size of 32×32 pixels. The convergence criterion for the adaptive PIV algorithm is set to 0.01 pixels for all cases. The laser pulse interval is adjusted such that the mean particle displacement is of the order of several pixels.

For each DR setting, two sets of measurements are conducted using different fields of view (FOVs). Large-FOV measurements yield the spatial distributions and scale dependence of turbulence statistics. Small-FOV measurements are conducted to examine small-scale characteristics. Since the pixel resolution is fixed, a smaller FOV results in a higher spatial resolution. The large FOV is illustrated by the green dashed rectangular frame in Fig. 1, located in the x–y plane, centered at the origin O, with dimensions of approximately 120×75 mm. For the large-FOV measurements, the camera is equipped with a macro lens (Nikon, AI AF Micro Nikkor 105 mm F2.8D). The small FOV has dimensions of approximately 40 × 25 mm and is illustrated by the red solid rectangle in Fig. 1. The small FOV is centered at the location $(x, y, z) = (0, 0, 120\text{ mm})$, with the offset of 120 mm corresponding to twice the fan pitch. For the small-FOV measurements, an additional extension tube set (Meike, MK-N-AF1-A) is mounted in conjunction with the macro lens. The spanwise offset of the small-FOV measurements is a compromise imposed by the camera working distance. Because the fan rotational speed is the same for all fans at the same height, this spanwise offset has minimal influence on the measured velocity statistics.

Measurements are repeated 8–12 times for each case to obtain more than 1000 velocity snapshots. The sampling interval corresponding to a sampling rate of 15 Hz is 0.067 s, which is comparable to the characteristic timescale of large-scale turbulent motions and much larger than that of small-scale turbulent motions. However, the present analyses are based on ensemble averages of instantaneous velocity fields and do not rely on time-series information. Therefore, the sampling interval does not affect the present statistics, although it would be insufficient for analyses of temporal evolution, such as temporal tracking of shear layers or velocity time derivatives. The time interval between the two particle images used to evaluate each instantaneous velocity field is the laser pulse interval, approximately 100–200 μs, which is adjusted for each fan-speed condition to satisfy the particle-displacement requirement and is much shorter than the turbulence timescale. An ensemble average over all snapshots is applied to evaluate turbulence statistics. The average value of f is denoted by $\langle f \rangle(x, y)$. The velocity fluctuations are denoted by $u = U - \langle U \rangle$ and $v = V - \langle V \rangle$. The present study also applies spatial averages within the FOV in the discussion of the general flow characteristics, rather than spatial distributions.

Because the present measurements are limited to two in-plane velocity components on an x–y plane, the following analysis characterizes the in-plane signatures of shear layers rather than their full three-dimensional geometry. Comparisons between two- and three-dimensional analyses of shear layers using DNS data of isotropic turbulence showed that two-dimensional analysis underestimates the absolute shear intensity and velocity jump because the out-of-plane components are not included, but captures the scale dependence and the main conditional characteristics of shear layers [26]. Therefore, the absolute magnitude of the shear intensity should be interpreted with this limitation in mind, whereas the scale dependence discussed below is expected to be less sensitive to the two-dimensional measurement limitation.

3. Shear layer analyses with the triple decomposition

3.1. Triple decomposition

The shear-layer analyses are conducted using the triple decomposition, which is useful for quantifying shearing motion. The present analyses follow those conducted for nearly homogeneous isotropic turbulence in our previous experiments with a turbulence wind tunnel [26]. The decomposition is applied to the low-pass-filtered velocity to examine the scale dependence of shear layers. A Gaussian low-pass filter is applied to the velocity fluctuation fields [47]:

$$\tilde{u}(x, y; L_F) = \int_{y-L_F}^{y+L_F} \int_{x-L_F}^{x+L_F} G(r, L_F) u(x', y') \mathrm{d}x' \mathrm{d}y', \tag{1}$$

$$\tilde{v}(x, y; L_F) = \int_{y-L_F}^{y+L_F} \int_{x-L_F}^{x+L_F} G(r, L_F) v(x', y') \mathrm{d}x' \mathrm{d}y', \tag{2}$$

$$r = \sqrt{(x - x')^2 + (y - y')^2}, \tag{3}$$

$$G(r, L_F) = \sqrt{\frac{6}{\pi L_F^2}} \exp\left(-\frac{6r^2}{L_F^2}\right). \tag{4}$$

The cutoff length L_F is determined from the Kolmogorov scale $\eta = (\nu^3/\varepsilon)^{1/4}$, which is defined using the kinematic viscosity ν and the turbulent kinetic energy dissipation rate ε. The integral in the filtering operation is truncated to the region $x \pm L_F$ and $y \pm L_F$ around the point (x, y). $G(|r| = L_F)$ is less than 0.25% of its peak value at $r = 0$, and extending the integration range does not affect the results presented here [26]. From the two-dimensional profiles of (u, v) measured in the small FOV, the dissipation rate is evaluated under the local-isotropy assumption [48]:

$$\varepsilon = \nu \left\langle 4\left(\frac{\partial u}{\partial x}\right)^2 + 4\left(\frac{\partial v}{\partial y}\right)^2 + 3\left(\frac{\partial u}{\partial y}\right)^2 + 3\left(\frac{\partial v}{\partial x}\right)^2 + 4\left(\frac{\partial u}{\partial x}\right)\left(\frac{\partial v}{\partial y}\right) + 6\left(\frac{\partial u}{\partial y}\right)\left(\frac{\partial v}{\partial x}\right) \right\rangle \tag{5}$$

The spatially averaged value of ε is used to evaluate the Kolmogorov scale. The cutoff length is given by $L_F = C_F \eta$, with $C_F = 20$–80. Quantities calculated from the filtered velocity fields are denoted by a tilde, e.g., $\tilde{\omega}$.

Equation (5) estimates the dissipation rate from the four in-plane velocity-gradient components available from the present two-dimensional two-component PIV measurements. Here, the local-isotropy assumption is used mainly to estimate the order of magnitude of ε and the Kolmogorov scale η, which defines the filter range. Therefore, possible uncertainty in ε affects the exact numerical value of η but does not alter the qualitative conclusions drawn from the scale dependence and orientation dependence of the conditionally averaged shear-layer statistics.

The triple decomposition is applied to the filtered velocity gradient tensor $\nabla\tilde{\boldsymbol{u}}$, whose components are denoted by $(\nabla\tilde{\boldsymbol{u}})_{ij} = \partial\tilde{u}_i/\partial x_j$, where the subscripts indicate tensor and vector components. The triple decomposition separates $\nabla\tilde{\boldsymbol{u}}$ into three components associated with shear (S), rigid-body rotation (R), and elongation (E), such that $\nabla\tilde{\boldsymbol{u}} = \nabla\tilde{\boldsymbol{u}}_S + \nabla\tilde{\boldsymbol{u}}_R + \nabla\tilde{\boldsymbol{u}}_E$. The decomposition algorithm is the same as that used in previous studies [10, 26, 49]. The decomposition is performed in the basic reference frame, in which the formula given below effectively extracts shear. The orthogonal transformation matrix from the laboratory frame $\boldsymbol{x}$ to the basic reference frame (BRF) $\boldsymbol{x}_B$ is denoted by $\boldsymbol{Q}_B$, which is determined from the eigenvectors of the rate-of-strain tensor $S_{ij} = (\partial\tilde{u}_i/\partial x_j + \partial\tilde{u}_j/\partial x_i)/2$ [10, 26, 49].

The velocity gradient tensor in the BRF is evaluated as $\nabla\tilde{\boldsymbol{u}}^{(B)} = \boldsymbol{Q}_B \nabla\tilde{\boldsymbol{u}} \boldsymbol{Q}_B^T$, where $\boldsymbol{Q}_B^T$ is the transpose of $\boldsymbol{Q}_B$. The decomposition formulae in the BRF are written as

$$\left(\nabla\tilde{\boldsymbol{u}}_{RES}^{(B)}\right)_{ij} = \mathrm{sgn}\left[\left(\nabla\tilde{\boldsymbol{u}}^{(B)}\right)_{ij}\right] \min\left[\left|\left(\nabla\tilde{\boldsymbol{u}}^{(B)}\right)_{ij}\right|, \left|\left(\nabla\tilde{\boldsymbol{u}}^{(B)}\right)_{ji}\right|\right], \tag{6}$$

$$\left(\nabla\tilde{\boldsymbol{u}}_{S}^{(B)}\right)_{ij} = \left(\nabla\tilde{\boldsymbol{u}}^{(B)}\right)_{ij} - \left(\nabla\tilde{\boldsymbol{u}}_{RES}^{(B)}\right)_{ij}, \tag{7}$$

$$\left(\nabla\tilde{\boldsymbol{u}}_{R}^{(B)}\right)_{ij} = \left[\left(\nabla\tilde{\boldsymbol{u}}_{RES}^{(B)}\right)_{ij} - \left(\nabla\tilde{\boldsymbol{u}}_{RES}^{(B)}\right)_{ji}\right]/2, \tag{8}$$

$$\left(\nabla\tilde{\boldsymbol{u}}_{E}^{(B)}\right)_{ij} = \left[\left(\nabla\tilde{\boldsymbol{u}}_{RES}^{(B)}\right)_{ij} + \left(\nabla\tilde{\boldsymbol{u}}_{RES}^{(B)}\right)_{ji}\right]/2, \tag{9}$$

These decomposed terms in the BRF are subsequently transformed back to the original laboratory coordinate system using the inverse of $\boldsymbol{Q}_B$.

3.2. Shear layer analyses

Shear-layer analyses are conducted at a given filter scale L_F to investigate the scale dependence of shear layers. Shear layers can be identified using the shear intensity defined as $\tilde{I}_S = \sqrt{2(\nabla\tilde{\boldsymbol{u}}_S)_{ij}(\nabla\tilde{\boldsymbol{u}}_S)_{ij}}$. Following previous studies of shear layers, the present study investigates the local flow fields in regions around the local maxima of $\tilde{I}_S$, which are located within shear layers. Here, local maxima with small $\tilde{I}_S$ values are excluded from the analyses to mitigate the effects of measurement errors. Specifically, local maxima satisfying $\tilde{I}_S > C_{th}\langle\tilde{I}_S\rangle$ are considered, with $C_{th} = 1.5$. Different values of C_{th} were also tested in Appendix A, but no significant changes in the scale dependence of shear layers were observed [26].

For each local maximum, a shear coordinate $\boldsymbol{x}_S = (\zeta_1, \zeta_2)$ aligned with the shear layer is introduced to evaluate conditional averages of shear layers. A quantity evaluated in the shear coordinate is denoted by a superscript (S). The directions of ζ_1 and ζ_2 are determined such that the shear component of the velocity gradient tensor $\nabla\tilde{\boldsymbol{u}}_S$ has only one non-zero component in the form

$$\nabla\tilde{\boldsymbol{u}}_S^{(S)} = \begin{pmatrix} 0 & -|\omega_S| \\ 0 & 0 \end{pmatrix}. \tag{10}$$

The transformation matrix from the laboratory coordinate to the shear coordinate, $\boldsymbol{Q}_S$, in $\boldsymbol{x}_S = \boldsymbol{Q}_S\boldsymbol{x}$, can be obtained by applying a 90° rotational transformation and/or a symmetric transformation matrix to $\boldsymbol{Q}_B$ [26].

Observations of the flow field in the shear coordinate provide a consistent evaluation of the local flow field around shear layers. For each shear layer, the shear coordinate is discretized using non-uniform grids, defined as

$$\zeta_i(n) = -\frac{\zeta_{\max}}{\alpha_\zeta} \arctan\left[\tanh(\alpha_\zeta)\left(1 - \frac{n+N_\zeta}{N_\zeta}\right)\right], \tag{11}$$

where $n = -N_\zeta, \dots, N_\zeta$ is the index of the discrete points, $N_\zeta = 100$ determines the spatial resolution, $\alpha_\zeta = 2.5$ is a stretching parameter controlling the non-uniformity, and $\zeta_{\max}$ defines the spatial extent of the discretized region. In the present study, $\zeta_{\max}$ is set to $7.5L_F$, as the filter is applied to identify shear layers at the scale of L_F. This non-uniform grid provides better spatial resolution near the shear-layer center. Flow variables, such as velocity and shear intensity, are interpolated onto the discretized shear coordinate using a third-order Lagrange polynomial interpolation scheme. The velocity vector in the shear coordinate is evaluated by applying the coordinate transformation to the velocity field. Here, the velocity components in the ζ_1 and ζ_2 directions are denoted by u_1 and u_2, respectively. The interpolation onto the shear coordinate is repeated for all local maximum locations. Ensemble averages over all shear layers, denoted by $\overline{f}$, are then taken as functions of (ζ_1, ζ_2).

The present analysis with two-dimensional velocity data characterizes the in-plane signatures of shear layers rather than their full three-dimensional topology. The term "shear layer" is used because previous three-dimensional analyses have shown that intense shearing motion is concentrated in layer-like structures [22, 23, 24, 50]. Moreover, DNS-based comparisons between two- and three-dimensional analyses showed that two-dimensional velocity data capture the shear-layer structure and its scale dependence, although the shear intensity and velocity jump are underestimated because the out-of-plane components are not included [26]. Thus, the present analysis is suitable for discussing the scale dependence of shear-layer characteristics, while the absolute magnitude of the shear intensity should be interpreted with this limitation in mind.

4. Results and discussion

4.1. Fundamental flow properties

Table 2 summarizes the velocity statistics obtained for each DR case. The velocity statistics are evaluated using both ensemble averages and spatial averages within the FOV to provide the overall flow properties. The mean velocities, $\langle U \rangle$ and $\langle V \rangle$, and the rms velocity fluctuations, $u_{rms} = \langle u^2 \rangle^{1/2}$ and $v_{rms} = \langle v^2 \rangle^{1/2}$, are evaluated from the large-FOV measurements. The mean velocity is comparable to the rms velocity fluctuations, and the mean flow is very weak compared with that in other wind-tunnel facilities. For Cases 1 and 2, u_{rms} is comparable to v_{rms}, and the velocity fluctuations are nearly isotropic. For Case 3, u_{rms} is about 1.4 times larger than v_{rms}. This case adopts different DRs that change from 0 to 100% at the central fan row. It is expected that the x-directional velocity changes drastically

Table 2
Summary of flow statistics. Results from the large FOV are presented for the mean velocities, $\langle U \rangle$ and $\langle V \rangle$, and the rms velocity fluctuations, u_{rms} and v_{rms}. The turbulent kinetic energy dissipation rate ε is evaluated with Eq. (5) from the small-FOV measurements. The Taylor microscale $\lambda = u_{rms}/(\partial u/\partial x)_{rms}$, the Kolmogorov scale $\eta = (\nu^3/\varepsilon)^{1/4}$, and the turbulent Reynolds number $Re_\lambda = u_{rms}\lambda/\nu$ are also evaluated from the small FOV. Δ is the spatial resolution, defined as the side length of the minimum interrogation window. The statistics are evaluated using ensemble and spatial averages.

	Case 1	Case 2	Case 3
$\langle U \rangle$ (m/s)	0.10	-0.28	0.52
$\langle V \rangle$ (m/s)	-0.28	-0.10	-1.03
u_{rms} (m/s)	0.47	0.39	0.97
v_{rms} (m/s)	0.42	0.40	0.71
u_{rms}/v_{rms}	1.12	0.98	1.37
ε (m^2/s^3)	3.0	1.2	12.7
λ (m)	4.0×10^{-3}	5.3×10^{-3}	4.0×10^{-3}
η (m)	1.9×10^{-4}	2.4×10^{-4}	1.3×10^{-4}
Re_λ	1.2×10^2	1.3×10^2	2.4×10^2
Δ/η for small FOV	2.7	2.1	3.8
Δ/η for large FOV	8.1	6.3	11.4

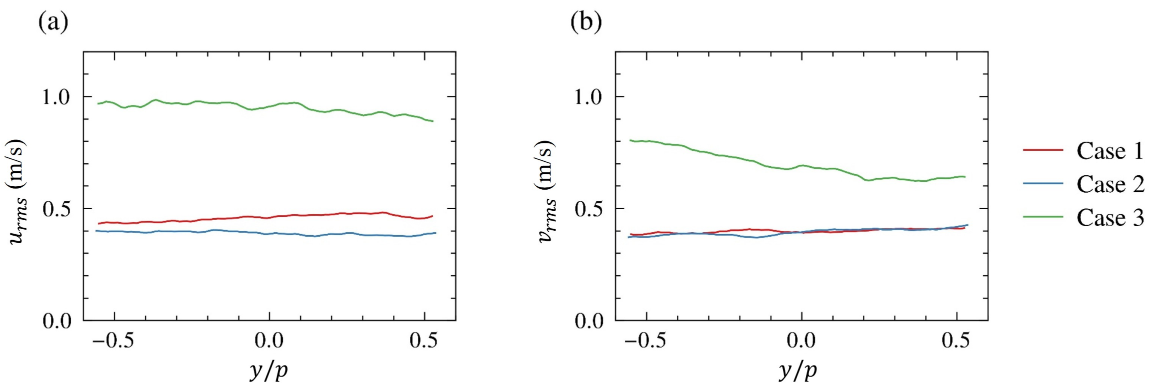

Figure 2: Vertical profiles of the rms velocity fluctuations in the (a) x direction (u_{rms}) and (b) y direction (v_{rms}) at $x = 0$. Results from the large-FOV measurements are presented.

in the y direction near the fan. Therefore, turbulence is produced by the mean velocity gradient $\partial\langle U \rangle/\partial y$. As also observed in other turbulent shear flows, turbulent production associated with $\partial\langle U \rangle/\partial y$ results in larger u_{rms} than the other components [47].

Table 2 also presents statistics related to velocity gradients evaluated from the small-FOV measurements. The Taylor microscale is evaluated using the x-directional velocity as $\lambda = u_{rms}/(\partial u/\partial x)_{rms}$. The Kolmogorov scale is calculated as $\eta = (\nu^3/\varepsilon)^{1/4}$ using the turbulent kinetic energy dissipation rate evaluated with Eq. (5). The turbulent Reynolds number defined with λ is $Re_\lambda = u_{rms}\lambda/\nu$, which exceeds 100 for all cases. Because of the large velocity fluctuations, Re_λ is large in Case 3. The spatial resolution Δ is defined as the side length of the interrogation window. For the large-FOV measurements, Δ is 6–11 times the Kolmogorov scale η. The shear-layer analyses below focus on scales greater than 20η, which are well captured by the present large-FOV PIV measurements.

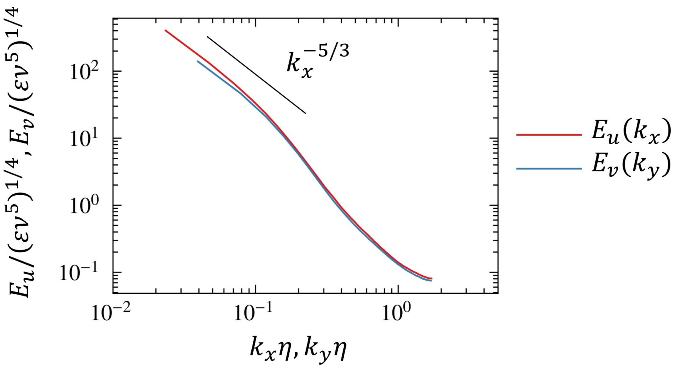

Figure 3: Longitudinal energy spectra $E_u(k_x)$ and $E_v(k_y)$ for Case 3. Results from the small-FOV measurements are presented.

Figure 2 presents the vertical profiles of the rms velocity fluctuations, u_{rms} and v_{rms}. The anisotropy discussed on the basis of spatial averages is observed at different vertical positions. Cases 1 and 2 exhibit better uniformity in the y direction than Case 3, which is the most anisotropic case.

Figure 3 shows the longitudinal energy spectra of u and v, which are denoted by $E_u(k_x)$ and $E_v(k_y)$, respectively, for Case 3, where k_x and k_y are the wavenumbers in the x and y directions, respectively. Although Case 3 exhibits large-scale anisotropy, as indicated by $u_{rms}/v_{rms} = 1.37$, the two spectra nearly collapse at high wavenumbers. This result indicates that the directional dependence of the velocity fluctuations becomes weak at small scales, which is consistent with the local-isotropy assumption used to estimate the order of η. This behavior is also consistent with observations in other turbulent flows with large-scale anisotropy, which exhibit less pronounced anisotropy at smaller scales [51]. Nevertheless, the present two-dimensional two-component PIV measurements do not provide all out-of-plane velocity-gradient components. The spectra therefore support, but do not fully validate, the local-isotropy estimate of ε. In the present study, this estimate is used mainly to set the filter scales, and the main conclusions are based on the relative scale dependence and orientation dependence of the shear-layer statistics. In addition, the collapse of $E_u(k_x)$ and $E_v(k_y)$ at high wavenumbers also suggests that the influence of the unmeasured out-of-plane components on the present two-dimensional shear-layer analysis is expected to be similar to that reported in the DNS-based comparison between two- and three-dimensional analyses in isotropic turbulence [26].

The filter range $L_F/\eta = 20$–80 of the low-pass filter corresponds to the representative dimensionless wavenumber range $k\eta = 2\pi\eta/L_F = 0.31$–$0.079$. The energy spectra in Fig. 3 approximately follow the $-5/3$ law for normalized wavenumbers smaller than $k\eta \approx 0.1$. Thus, the analyzed scales extend from the dissipation-range side to the inertial-range side [47]. Since η is evaluated from the dissipation rate estimated under the local-isotropy assumption, these values are used only as approximate indicators of the spectral location of the filter scales. The present discussion therefore focuses on the scale dependence over $L_F/\eta = 20$–80, rather than on a precise classification of each scale.

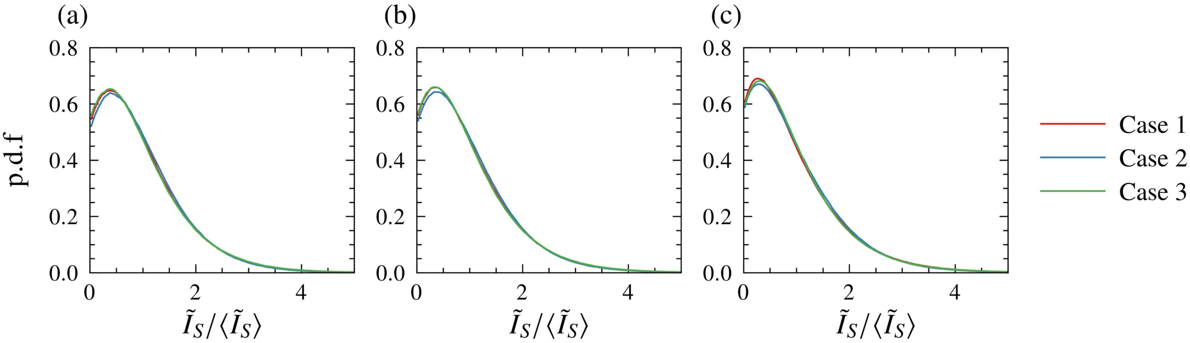

Figure 4: Probability density functions of the shear intensity $\tilde{I}_S$ for Cases 1–3 at (a) $L_F/\eta = 80$, (b) $L_F/\eta = 50$, and (c) $L_F/\eta = 20$.

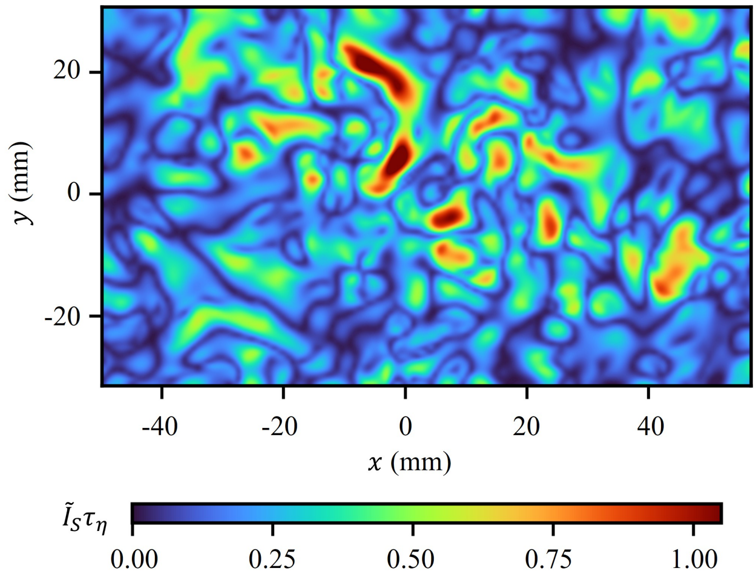

Figure 5: Instantaneous distribution of shear intensity $\tilde{I}_S$, normalized by the Kolmogorov timescale $\tau_\eta = \eta^2/\nu$, for Case 1 at the filter length $L_F = 20\eta$.

Figure 4 shows the probability density functions of the shear intensity $\tilde{I}_S$ for $L_F/\eta = 80$, 50, and 20. At each filter size, the pdfs for Cases 1–3 almost overlap. This indicates that the probability of observing intense shear regions is only weakly affected by the large-scale anisotropy examined here.

4.2. Conditionally averaged properties of shear layers

Figure 5 shows the distribution of shear intensity $\tilde{I}_S$ for the filter length $L_F = 20\eta$ in Case 1. Regions with high values of $\tilde{I}_S\tau_\eta$ often appear in layer-like patterns, consistent with previous observations [26]. The shear intensity takes non-zero values at almost all locations, indicating that shearing motion persists throughout the flow.

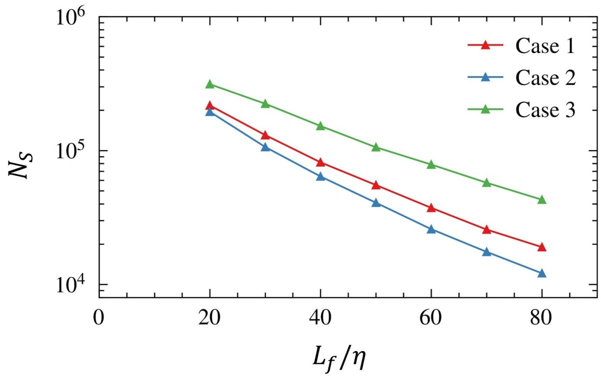

Figure 6: Number of detected shear-layer samples, N_S, as a function of the filter size.

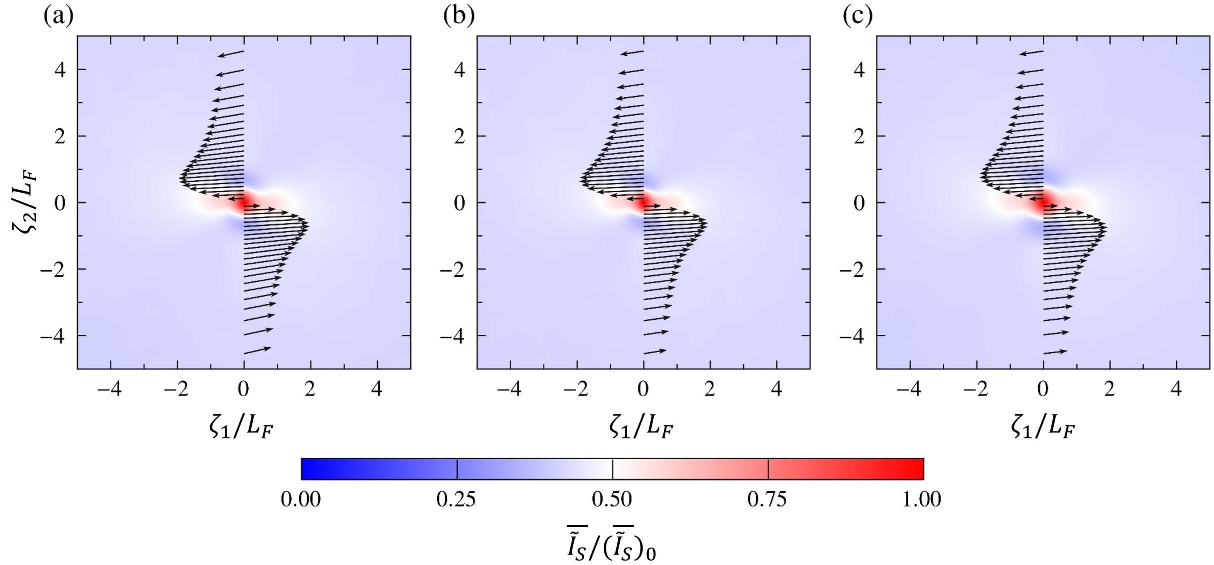

Figure 7: Conditionally averaged shear-intensity profiles around shear layers at the filter length $L_F = 20\eta$ for (a) Case 1, (b) Case 2, and (c) Case 3. The arrows represent the conditionally averaged velocity vector at $\zeta_1 = 0$.

Figure 6 shows the number of shear-layer samples, N_S, used to evaluate the conditional statistics, as a function of the filter size. The number of samples decreases with increasing L_F/η, because larger filters extract larger structures and reduce the number of local maxima of $\tilde{I}_S$ within the measurement region. Nevertheless, even at the largest filter size examined here, N_S remains larger than 10^4 for all cases. A previous study reported conditionally averaged shear-layer statistics using sample numbers between 10^3 and 10^7, and showed that the mean shear-layer properties were insensitive to the sample number over this range [23]. Therefore, the present sample number is considered sufficient for evaluating the conditionally averaged shear-layer statistics.

The following profiles are obtained by conditional ensemble averaging around detected shear layers after alignment with the shear coordinate system. Figure 7 shows the conditionally averaged shear-intensity profiles around shear

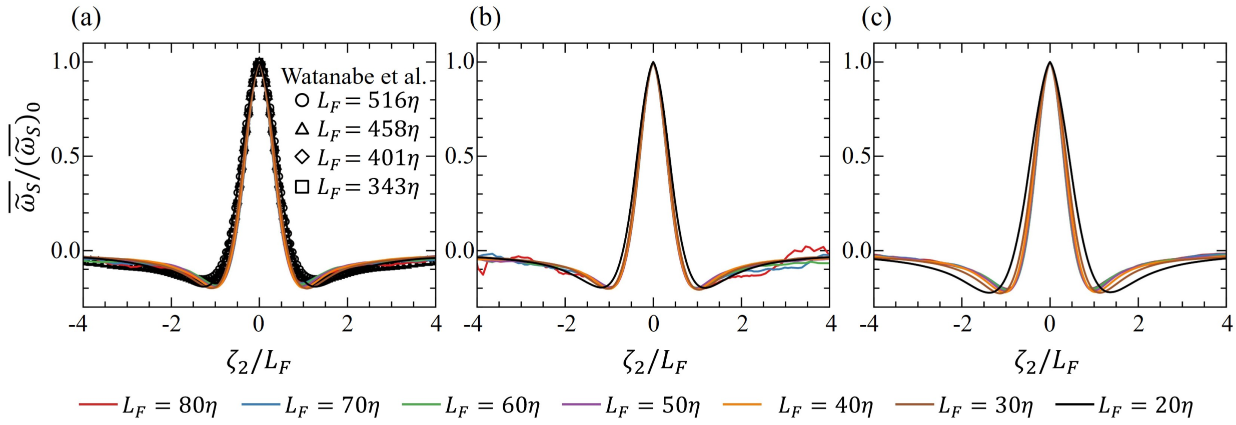

Figure 8: Conditionally averaged shear-vorticity profiles across shear layers in (a) Case 1, (b) Case 2, and (c) Case 3 at different filter sizes. The experimental results for decaying nearly homogeneous isotropic turbulence generated by multiple-jet interaction are also compared with those of Case 1 [26].

layers, evaluated in the shear coordinate. The color contours represent (2-4) the conditionally averaged shear intensity normalized by its value at $(\zeta_1, \zeta_2) = (0, 0)$, $(\overline{\tilde{I}_S})_0$. The conditionally averaged velocity vectors at $\zeta_1 = 0$ are also shown to indicate the flow direction. The conditionally averaged shear intensity exhibits a clear layer-like structure, with variation more pronounced in the ζ_2 direction than in the ζ_1 direction. The conditionally averaged vectors also show that the shear arises from the gradient of the ζ_1-directional velocity in the ζ_2 direction. As the distance from the layer center increases, the shear intensity decreases. The conditionally averaged shear intensity and conditionally averaged velocity vectors show similar distributions in both the isotropic cases (Cases 1 and 2) and the anisotropic case (Case 3).

Figure 8 shows the variations of the conditionally averaged shear vorticity $\overline{\tilde{\omega}_S}$, normalized by its center value $(\overline{\tilde{\omega}_S})_0$, in the ζ_2 direction at $\zeta_1 = 0$, namely across the shear layer. For each case, the results for different filter lengths L_F are plotted against ζ_2/L_F. At large $|\zeta_2|$ outside the shear layer, the conditionally averaged shear vorticity oscillates because of the limited number of samples at large $|\zeta_2|$ for large filter sizes. The conditionally averaged shear-vorticity profiles obtained in decaying nearly homogeneous isotropic turbulence generated by multiple-jet interaction [26] are also compared with those of Case 1, which is the most isotropic case among the present experimental conditions. The previous experiment was conducted at much higher turbulent Reynolds numbers ($Re_\lambda = 400$–800), and the filter size normalized by the Kolmogorov scale was much larger than that in the present study. Nevertheless, the compared scales were still located in the inertial subrange. The normalized shear-vorticity profile across the shear layer is consistent with the present result. This agreement supports the reliability of the present conditional averaging procedure and indicates that the normalized shear-vorticity distribution across the layer agrees with that reported in a different turbulent flow at a higher Reynolds number.

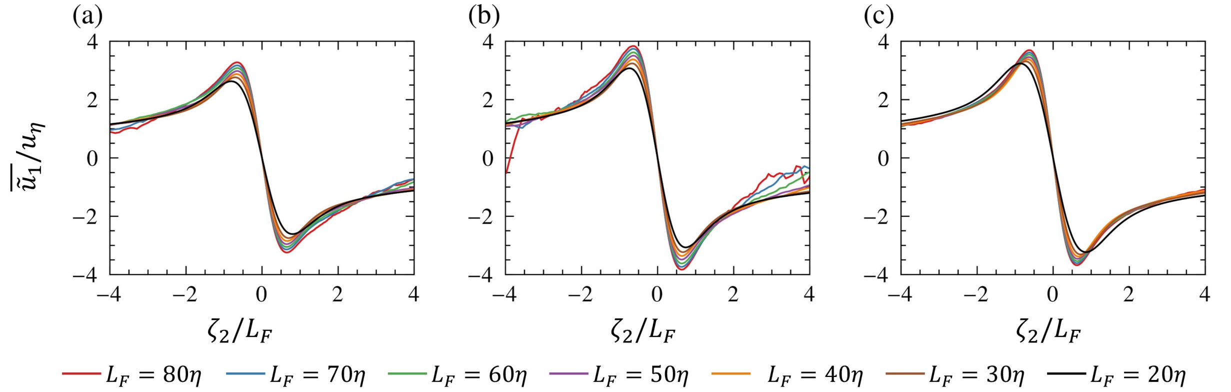

Figure 9: Profiles of the conditionally averaged ζ_1-directional velocity $\tilde{u}_1$ normalized by the Kolmogorov velocity $u\eta$ across shear layers in (a) Case 1, (b) Case 2, and (c) Case 3 at different filter sizes.

Nonetheless, the conditionally averaged shear-vorticity profile does not depend on L_F for $L_F/\eta \geq 30$, indicating that the shear layer exhibits self-similarity in all cases, including both isotropic and anisotropic conditions. The profile for $L_F/\eta = 20$ in Fig. 8 shows a slight deviation from those at larger filter sizes. Since this is the smallest filter size examined here and is closest to the dissipation range, greater viscous effects associated with the smaller filter may contribute to this deviation. However, the present data do not allow us to identify the precise cause.

Figure 9 shows the conditionally averaged velocity in the ζ_1 direction, $\overline{\tilde{u}_1}$, across the shear layer. The mean velocity changes significantly across the shear layer. This mean velocity jump is observed in the layer where $(\overline{\tilde{\omega}_S})$ is locally large. The jump becomes larger as the scale increases, and larger-scale shear layers are associated with a greater velocity change across the shear layer.

The mean properties of shear layers are evaluated using conditional statistics. The aspect ratio of shear layers is evaluated from $\overline{\tilde{\omega}_S}/(\overline{\tilde{\omega}_S})_0$. The shear-layer extent in the ζ_1 direction, $L_{\zeta 1}$, is defined as the distance between two points with $\overline{\tilde{\omega}_S}/(\overline{\tilde{\omega}_S})_0 = 0.1$ at $\zeta_2 = 0$. Similarly, the layer extent in the ζ_2 direction, $L_{\zeta 2}$, is defined as the distance between two points with $\overline{\tilde{\omega}_S}/(\overline{\tilde{\omega}_S})_0 = 0.1$ at $\zeta_1 = 0$. The aspect ratio is defined as $A_R = L_{\zeta 1}/L_{\zeta 2}$. The shear-layer thickness is evaluated from the profile of $\overline{\tilde{\omega}_S}/(\overline{\tilde{\omega}_S})_0$ in the ζ_2 direction. The thickness δ_S is defined as the half-width of $\overline{\tilde{\omega}_S}/(\overline{\tilde{\omega}_S})_0$, namely the distance between two points where $\overline{\tilde{\omega}_S}/(\overline{\tilde{\omega}_S})_0 = 0.5$ at $\zeta_1 = 0$. The thickness is proportional to the filter length L_F, as the filter is applied to investigate shear layers at the scale of L_F. The mean velocity jump across the shear layer, Δu, is defined as $\Delta u = \delta_S(\overline{\tilde{\omega}_S})_0$, where $(\overline{\tilde{\omega}_S})_0$ is equivalent to the mean velocity gradient across the shear layer.

Figure 10 presents the aspect ratio A_R of shear layers as a function of scale. For all cases, $A_R \approx$ 4–5 and varies little with scale. This value of A_R is consistent with results obtained for nearly homogeneous isotropic turbulence generated by the interaction of supersonic jets [52], and remains unchanged even in Case 3, which is the most anisotropic case with a large u_{rms}/v_{rms}.

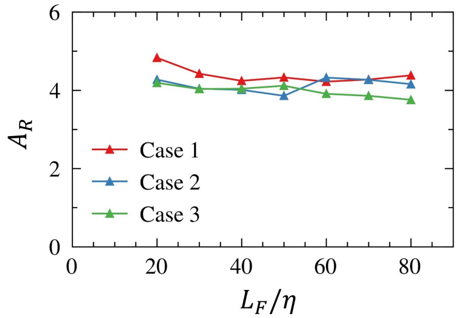

Figure 10: Aspect ratio of shear layers.

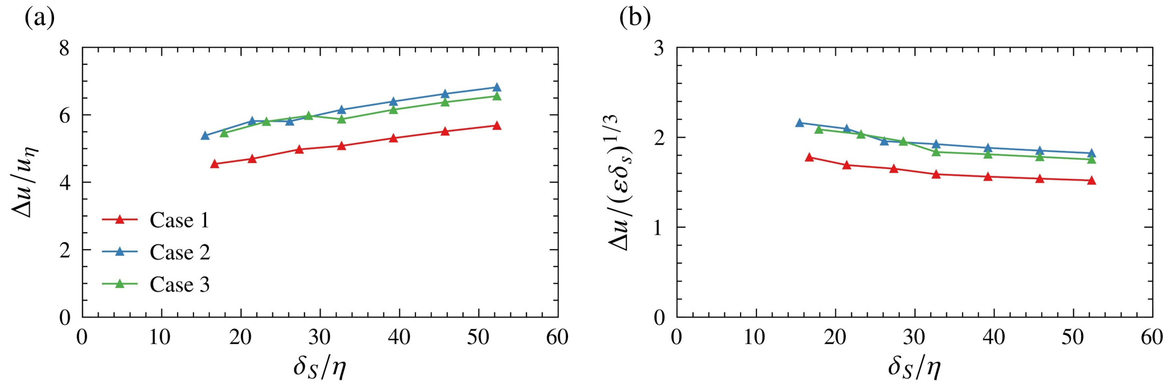

Figure 11: Velocity jump across shear layers evaluated from conditional averages, normalized by (a) the Kolmogorov velocity u_η and (b) $(\varepsilon\delta_S)^{1/3}$.

Figure 11(a) shows the mean velocity jump across the shear layer, Δu, normalized by the Kolmogorov velocity $u_\eta = (\nu\varepsilon)^{1/4}$ and plotted against the shear-layer thickness δ_S normalized by the Kolmogorov scale η. The mean velocity jump gradually increases with increasing scale. The present study investigates shear layers at scales above 20η. Shear layers at the smallest scale have a thickness of about 5η and a mean velocity jump of about 4–$5u_\eta$ [23]. Extrapolation of the data points in Fig. 11(a) also suggests that $\Delta u/u_\eta$ is about 4–5 at $L_F/\eta \approx 5$, which is consistent with the properties of the smallest-scale shear layers.

In the inertial subrange, the scale dependence of Δu is predicted by Kolmogorov's second similarity hypothesis as $\Delta u \sim (\varepsilon\delta_S)^{1/3}$. Figure 11(b) plots Δu normalized by $(\varepsilon\delta_S)^{1/3}$. This normalized velocity jump depends only weakly on δ_S/η. The range of δ_S/η is not fully contained within the inertial subrange, as it is as small as $\delta_S/\eta \approx 20$. However, $\Delta u \sim (\varepsilon\delta_S)^{1/3}$ is only weakly influenced by viscous effects at scales smaller than the inertial range. In addition, this scaling is not affected by the anisotropy in Case 3.

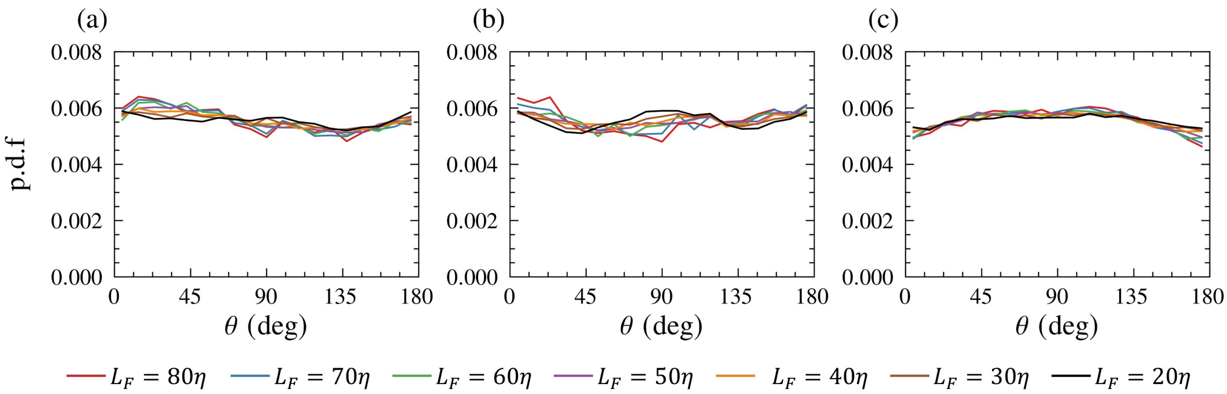

Figure 12: Probability density function of the angle θ between the shear-layer normal direction and the x direction: (a) Case 1, (b) Case 2, and (c) Case 3.

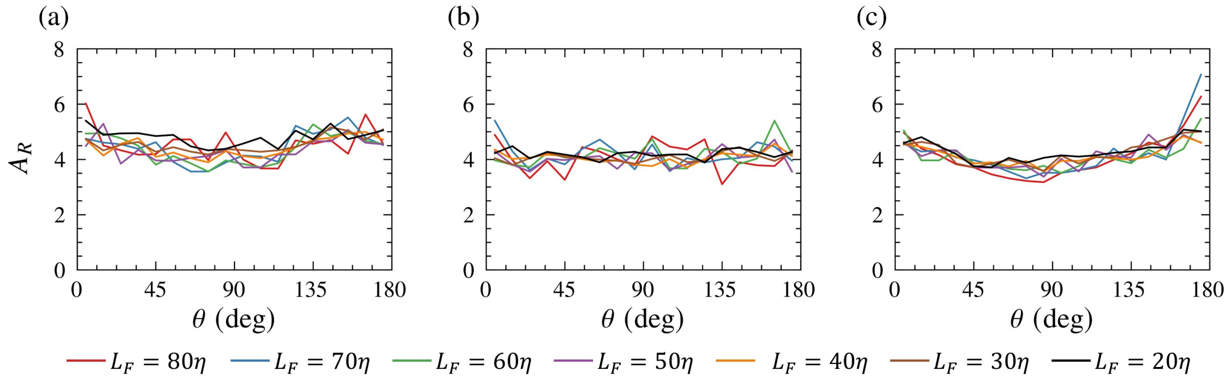

Figure 13: Aspect ratio of shear layers for different θ: (a) Case 1, (b) Case 2, and (c) Case 3.

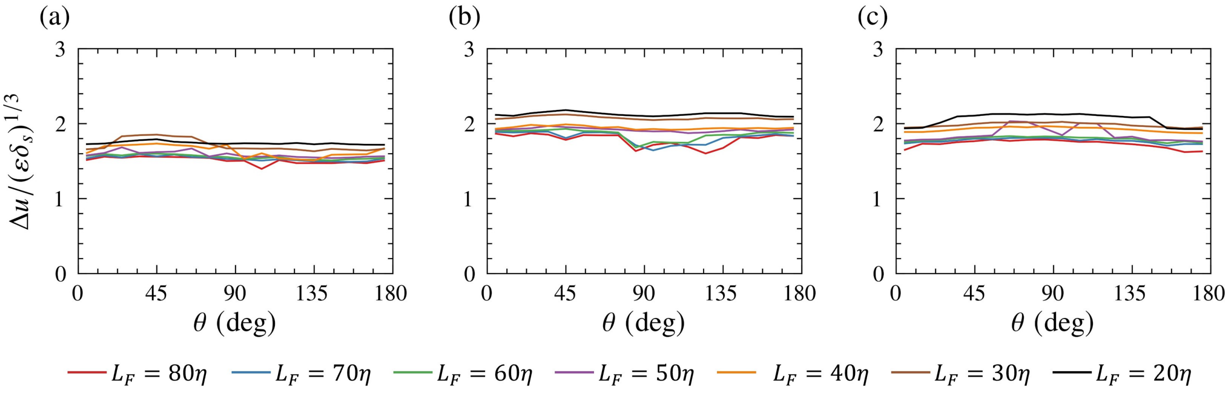

Figure 14: Mean velocity jump Δu, normalized by $(\varepsilon\delta_S)^{1/3}$, for different θ: (a) Case 1, (b) Case 2, and (c) Case 3.

4.3. Dependence of shear layers on orientation

The anisotropic velocity fluctuations in Case 3 may cause shear layers to align preferentially in a specific direction because the velocity fluctuations are larger in the x direction than in the y direction. Therefore, the dependence of shear layers on orientation is examined here. The orientation of a shear layer is defined as the angle of the ζ_2 direction of the shear coordinate measured from the x direction of the laboratory coordinate. The ζ_2 direction is perpendicular to the shear layer. Thus, $\theta = 0$ indicates that the shear layer is perpendicular to the x axis of the laboratory reference frame. Figure 12 shows the probability density function (pdf) of θ. The pdf is almost constant over all angles, indicating that the shear layers exhibit no preferential orientation regardless of the level of large-scale anisotropy.

This weak orientation dependence is consistent with the classical picture of local isotropy, in which sufficiently small-scale turbulent motions tend to become less dependent on the directionality imposed by the large-scale flow [53, 54, 55]. Although Case 3 exhibits anisotropic velocity fluctuations at large scales, the longitudinal energy spectra shown in Fig. 3 indicate that the directional difference becomes weak at small scales. The nearly uniform orientation pdf therefore suggests that the shear layers examined here, whose scales are of $O(10^1\eta)$, are governed mainly by local small-scale dynamics rather than by the anisotropic large-scale velocity fluctuations. This interpretation is also consistent with the weak orientation dependence of the aspect ratio and normalized velocity jump discussed below.

The conditional averages of shear layers are evaluated as functions of θ to examine the orientation dependence. The shear layers are divided into 18 groups according to θ, which is discretized between 0 and 180° with an interval of 10°. The angle-conditioned statistics are therefore used to identify systematic orientation trends rather than small differences between neighbouring angle bins. The θ-dependent characteristics of shear layers are calculated from statistics evaluated using the samples in each group. Figure 13 shows the aspect ratio obtained for shear layers with different angles. The aspect ratio is about 4–5 in Cases 1 and 2, and the shear-layer shape hardly changes with orientation. For Case 3, the aspect ratio is relatively small at $\theta \approx 90°$ and increases as θ departs from this value. When the shear layers are parallel to the x direction ($\theta \approx 90°$), they are slightly shorter in the layer-parallel direction. However, this θ dependence is not significant enough to alter the overall shear-layer pattern observed in Fig. 7. Figure 14 shows the mean velocity jump Δu, normalized by $(\varepsilon\delta_S)^{1/3}$, for shear layers with different angles. For all angles and scales, $\Delta u/(\varepsilon\delta_S)^{1/3}$ is between 1.8 and 2.1. The scaling of $\Delta u \sim (\varepsilon\delta_S)^{1/3}$ still holds for shear layers with different angles. It is possible that $u_{rms} > v_{rms}$ leads to a larger mean velocity jump Δu for shear layers that are parallel to the x direction, because such shear layers have a velocity jump arising from velocity in the x direction. However, the negligible θ dependence of Δu in Case 3 indicates that rms velocity fluctuations are irrelevant to the velocity jump of shear layers at scales of $O(10^1\eta)$. This implies that large-scale anisotropy does not affect the properties of shear layers at these scales, and that the prediction established for isotropic turbulence in previous studies remains valid even in anisotropic cases.

Although scalar fields were not measured in the present study, the present results have implications for scalar transport. Previous studies showed that the velocity field induced by shear layers makes a dominant contribution to turbulent scalar flux in turbulent jets [34], and that small-scale shear-layer instability enhances the dissipation of scalar fluctuations [50, 56, 35]. These findings indicate that shear layers are important for turbulent heat and mass transfer. The present results show that the geometrical and kinematic characteristics of shear layers are only weakly affected by the moderate large-scale anisotropy examined here. This suggests that the shearing motions relevant to scalar transport can remain similar even when the large-scale velocity fluctuations are anisotropic.

It should be noted that the anisotropy examined in the present study is limited to the moderate level represented by Case 3, for which $u_{rms}/v_{rms} = 1.37$. Therefore, the present results do not imply that shear-layer characteristics are unaffected by all forms of strong anisotropy. In wall-bounded turbulence and turbulent shear flows, direct effects of the wall or mean shear can influence the geometry and orientation of shear layers. For example, in turbulent jets, previous studies showed that the shear-layer orientation is influenced by the mean shear, especially near the outer edge of the jet [23, 57]. In such flows, it is difficult to separate the effect of anisotropic velocity fluctuations from the direct influence of the wall or mean shear. The present opposed multi-fan configuration provides anisotropic velocity fluctuations with relatively small mean velocity, and is therefore useful for examining the influence of anisotropic fluctuations on shear-layer characteristics. The present results indicate that, within this range of anisotropy and weak mean flow, the scale dependence and orientation dependence of the shear-layer statistics are only weakly affected by the large-scale anisotropy.

5. Conclusion

The present study investigated shear-layer structures in turbulence generated by opposed multiple-fan arrays using two-dimensional two-component PIV and the triple decomposition applied to filtered velocity fields. Measurements were conducted for three fan-speed conditions, including nearly isotropic and anisotropic cases, in order to examine the scale dependence and flow dependence of shear layers. The results showed that intense shearing motions form clear layer-like structures and that the conditionally averaged shear-vorticity profile exhibits self-similarity for filter scales above 30η within the investigated range from 20η to 80η.

The conditional statistics showed that the aspect ratio of shear layers remains approximately 4–5 and is only weakly dependent on scale. The mean velocity jump across shear layers increases with increasing scale and is approximately scaled by $(\varepsilon\delta_S)^{1/3}$, even though the examined scales are not fully within the inertial subrange. These characteristics were similar among all cases, including the anisotropic case with $u_{rms} > v_{rms}$, indicating that the fundamental properties of shear layers at scales of $O(10^1\eta)$ are not strongly affected by large-scale anisotropy.

The orientation dependence of shear layers was also examined. The probability density function of the shear-layer orientation was nearly uniform, showing no preferential alignment even in the anisotropic case. In addition, the normalized velocity jump exhibited minimal dependence on orientation, while a weak orientation dependence of the aspect ratio appeared only in the most anisotropic case. In that case, shear layers parallel to the fan-flow direction were slightly shorter in the layer-parallel direction, but this trend was too small to modify the overall shear-layer pattern. These results suggest that, within the moderate anisotropy and weak-mean-flow conditions examined here, the small-scale shear-layer structure is governed primarily by local dynamics rather than by the anisotropy of the large-scale velocity fluctuations. Overall, the present results indicate that shear layers retain common geometrical and kinematic features across the isotropic and anisotropic conditions examined here. This robustness is relevant to heat and mass transfer associated with shear layers [34, 35] because it suggests that the local kinematics governing scalar transport and mixing can remain similar even when the large-scale flow is anisotropic.

AI declaration

The authors used an AI-assisted language tool to improve readability, grammatical accuracy, spelling and clarity; all content was verified and approved by the authors, who take full responsibility for the text.

CRediT authorship contribution statement

Zexu Han: Data Curation, Formal Analysis, Investigation, Methodology, Validation, Visualization, Writing/Original Draft Preparation, Writing/Review & Editing . **Haruyuki Sakai:** Formal Analysis, Investigation, Methodology, Validation, Visualization, Writing/Review & Editing . **Tomoaki Watanabe:** Conceptualization, Data Curation, Formal Analysis, Funding Acquisition, Investigation, Methodology, Project Administration, Resources, Software, Supervision, Validation, Visualization, Writing/Original Draft Preparation, Writing/Review & Editing . **Koji Nagata:** Funding Acquisition, Methodology, Project Administration, Resources, Supervision, Validation, Visualization, Writing/Review & Editing .

Funding

This work was supported by JSPS KAKENHI Grant Nos. JP23K22669 and JP25K01155 and Kansai Research Foundation for Technology Promotion. Z. Han gratefully acknowledges financial support from the Amano Institute of Technology Scholarship.

Declaration of competing interest

The authors report no conflicts of interest.

Data availability

The data supporting the findings of this study are available from the corresponding author upon reasonable request.

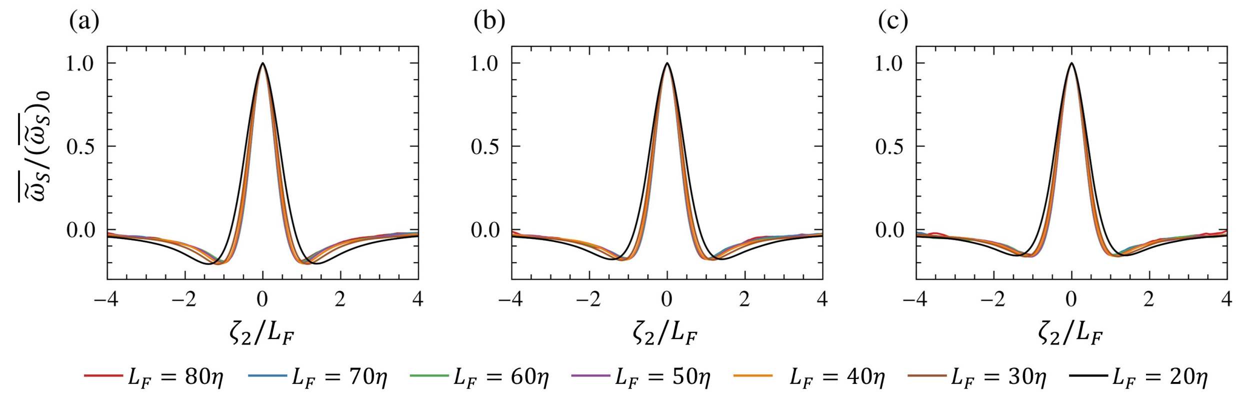

Figure 15: Conditionally averaged shear-vorticity profiles across shear layers in Case 3 for (a) $C_{th} = 2$, (b) $C_{th} = 3$, and (c) $C_{th} = 4$.

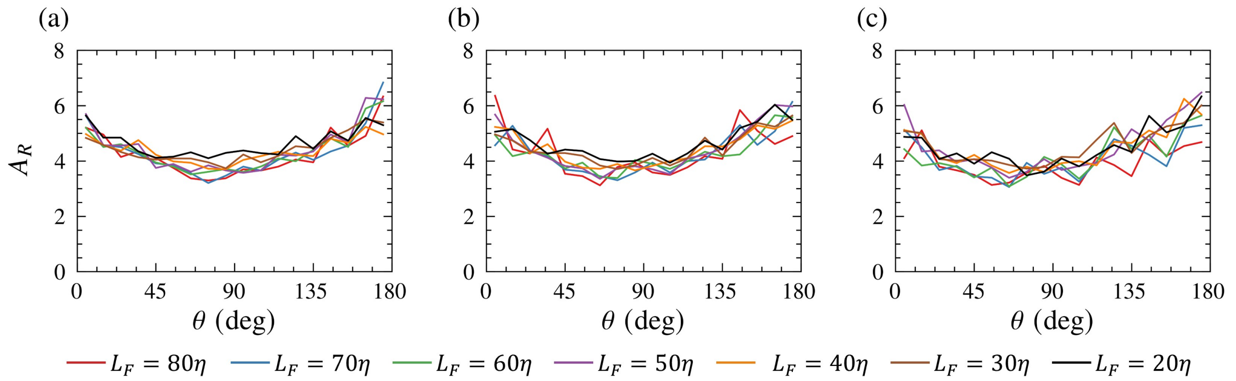

Figure 16: Aspect ratio of shear layers for different θ in Case 3 for (a) $C_{th} = 2$, (b) $C_{th} = 3$, and (c) $C_{th} = 4$.

A. Threshold dependence of shear-layer characteristics

The present study evaluates the statistics of shear layers identified using the threshold criterion $\tilde{I}_S > C_{th}\langle \tilde{I}_S \rangle$ with $C_{th} = 1.5$. As C_{th} increases, weaker shear layers are excluded from the statistical evaluation. This appendix examines the dependence of the shear-layer characteristics on C_{th}. Specifically, we test $C_{th} = 2$, 3, and 4 for Case 3.

Figure 15 shows the conditionally averaged shear-vorticity profiles across shear layers. Figures 16 and 17 show the aspect ratio and the normalized mean velocity jump evaluated from conditional averages for different shear-layer angles. The corresponding results for $C_{th} = 1.5$ are presented in Figs. 8(c), 13(c) and 14(c). The conditionally averaged shear-vorticity profiles, normalized by the center value of the shear layer and the filter size, change little with the threshold value. Similarly, the aspect ratio shows little variation with C_{th}. The mean velocity jump becomes larger as C_{th} increases because increasing C_{th} excludes weak shear layers from the statistical samples. However, its dependences on the filter size and angle remain nearly unchanged for different C_{th} values. Therefore, the present conclusions on the scaling and orientation dependence of the shear-layer characteristics are not affected by the specific choice of threshold.

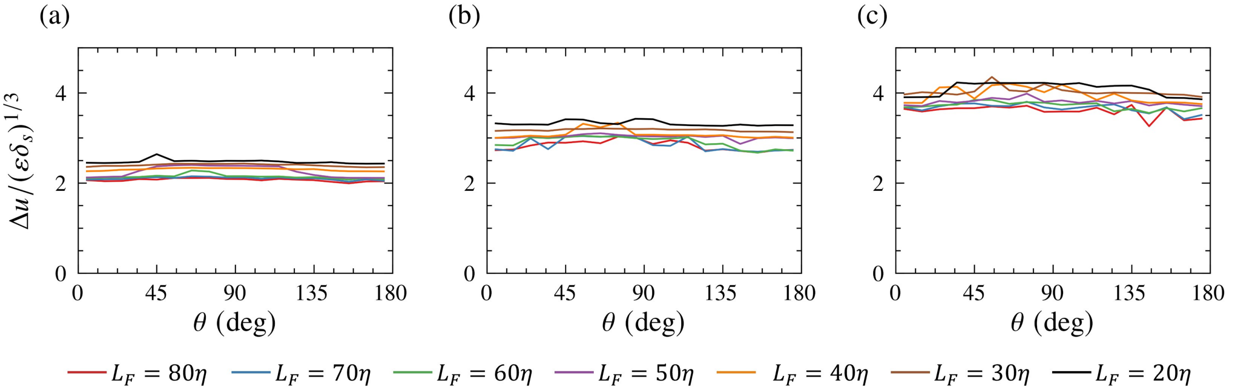

Figure 17: Mean velocity jump Δu, normalized by $(\varepsilon \delta_S)^{1/3}$, for different θ in Case 3 for (a) $C_{th} = 2$, (b) $C_{th} = 3$, and (c) $C_{th} = 4$.

References

[1] S. A. Thorpe, The near-surface ocean mixing layer in stable heating conditions, J. Geophys. Res. 83 (1978) 2875–2885.

[2] A. E. Gargett, Ocean turbulence, Annu. Rev. Fluid Mech. 21 (1989) 419–451.

[3] J. R. Garratt, The atmospheric boundary layer, Earth-Sci. Rev. 37 (1994) 89–134.

[4] L. Mahrt, Stratified atmospheric boundary layers, Boundary-Layer Meteorol. 90 (1999) 375–396.

[5] J. Liu, S. Hussain, W. Wang, G. Xie, B. Sundén, Experimental and numerical investigations of heat transfer and fluid flow in a rectangular channel with perforated ribs, Int. Commun. Heat Mass Transf. 121 (2021) 105083.

[6] C. Nuntadusit, M. Wae-Hayee, A. Bunyajitradulya, S. Eiamsa-Ard, Visualization of flow and heat transfer characteristics for swirling impinging jet, Int. Commun. Heat Mass Transf. 39 (2012) 640–648.

[7] A. Sikka, D. Singh, S. Chander, Flow dynamics and heat transfer characteristics of air/water mist jet impingement using Eulerian-Eulerian approach, Int. Commun. Heat Mass Transf. 159 (2024) 108003.

[8] K. Nagesha, Exploring turbulence and micro-scale mixing mechanisms for enhancing jet impingement heat transfer using micro-roughness elements: A data-driven and numerical analysis, Int. Commun. Heat Mass Transf. 162 (2025) 108646.

[9] A. Tsinober, An informal conceptual introduction to turbulence, Springer, 2009.

[10] V. Kolář, Vortex identification: New requirements and limitations, Int. J. Heat Fluid Flow 28 (2007) 638–652.

[11] P. A. Davidson, Turbulence: An Introduction for Scientists and Engineers, Oxford Univ. Pr., 2015.

[12] J. Jeong, F. Hussain, On the identification of a vortex, J. Fluid Mech. 285 (1995) 69–94.

[13] J. Jiménez, A. A. Wray, On the characteristics of vortex filaments in isotropic turbulence, J. Fluid Mech. 373 (1998) 255–285.

[14] C. B. da Silva, R. J. N. Dos Reis, J. C. F. Pereira, The intense vorticity structures near the turbulent/non-turbulent interface in a jet, J. Fluid Mech. 685 (2011) 165–190.

[15] M. Tanahashi, S. Iwase, T. Miyauchi, Appearance and alignment with strain rate of coherent fine scale eddies in turbulent mixing layer, J. Turbulence 2 (2001) 1–18.

[16] R. Jahanbakhshi, N. S. Vaghefi, C. K. Madnia, Baroclinic vorticity generation near the turbulent/non-turbulent interface in a compressible shear layer, Phys. Fluids 27 (2015) 105105.

[17] T. Watanabe, C. B. da Silva, K. Nagata, Y. Sakai, Geometrical aspects of turbulent/non-turbulent interfaces with and without mean shear, Phys. Fluids 29 (2017) 085105.

[18] T. Watanabe, R. Jaulino, R. R. Taveira, C. B. da Silva, K. Nagata, Y. Sakai, Role of an isolated eddy near the turbulent/non-turbulent interface layer, Phys. Rev. Fluids 2 (2017) 094607.

[19] A. A. Ghira, G. E. Elsinga, C. B. da Silva, Characteristics of the intense vorticity structures in isotropic turbulence at high Reynolds numbers, Phys. Rev. Fluids 7 (2022) 104605.

[20] A. A. Ghira, G. E. Elsinga, C. B. da Silva, Lifetime of the intense vorticity structures in isotropic turbulence, J. Fluid Mech. 1007 (2025) A62.

[21] A. Vincent, M. Meneguzzi, The dynamics of vorticity tubes in homogeneous turbulence, J. Fluid Mech. 258 (1994) 245–254.

[22] T. Watanabe, K. Tanaka, K. Nagata, Characteristics of shearing motions in incompressible isotropic turbulence, Phys. Rev. Fluids 5 (2020) 072601(R).

[23] M. Hayashi, T. Watanabe, K. Nagata, Characteristics of small-scale shear layers in a temporally evolving turbulent planar jet, J. Fluid Mech. 920 (2021) A38.

[24] D. Fiscaletti, O. R. H. Buxton, A. Attili, Internal layers in turbulent free-shear flows, Phys. Rev. Fluids 6 (2021) 034612.

[25] T. Watanabe, H. Abreu, K. Nagata, C. B. da Silva, Small-scale shear layers in isotropic turbulence of viscoelastic fluids, J. Fluid Mech. 1005 (2025) A14.

[26] T. Watanabe, T. Mori, K. Ishizawa, K. Nagata, Scale dependence of local shearing motion in decaying turbulence generated by multiple-jet interaction, J. Fluid Mech. 997 (2024) A14.

[27] R. Arun, T. Colonius, Velocity gradient partitioning in turbulent flows, J. Fluid Mech. 1000 (2024) R5.

[28] R. Arun, M. Kamal, T. Colonius, P. L. Johnson, Normality-based analysis of multiscale velocity gradients and energy transfer in direct and large-eddy simulations of isotropic turbulence, J. Fluid Mech. 1021 (2025) A47.

[29] T. Watanabe, Y. Sakai, K. Nagata, O. Terashima, H. Suzuki, T. Hayase, Y. Ito, Visualization of turbulent reactive jet by using direct numerical simulation, Int. J. Model. Simul. Sci. Comput. 4 (2013) 1341001.

[30] O. Terashima, Y. Sakai, Y. Goto, K. Onishi, K. Nagata, Y. Ito, On the turbulent energy transport related to the coherent structures in a planar jet, Exp. Therm. Fluid Sci. 68 (2015) 697–710.

[31] O. Terashima, Y. Sakai, Y. Ito, Measurement of fluctuating temperature and POD analysis of eigenmodes in a heated planar jet, Exp. Therm. Fluid Sci. 92 (2018) 113–124.

[32] I. Di Venuta, A. Boghi, M. Angelino, F. Gori, Passive scalar diffusion in three-dimensional turbulent rectangular free jets with numerical evaluation of turbulent prandtl/schmidt number, Int. Commun. Heat Mass Transf. 95 (2018) 106–115.

[33] I. Di Venuta, A. Boghi, M. Angelino, I. Petracci, F. Gori, Numerical simulation and self-similarity of the mean mass transfer in turbulent round jets, Int. Commun. Heat Mass Transf. 122 (2021) 105146.

[34] R. Enoki, T. Watanabe, K. Nagata, Statistical properties of shear and nonshear velocity components in isotropic turbulence and turbulent jets, Phys. Rev. Fluids 8 (2023) 104602.

[35] T. Watanabe, K. Nagata, Influences of small-scale shear instability on passive-scalar mixing in a shear-free turbulent front, J. Fluid Mech. 1008 (2025) A20.

[36] M. M. Rogers, P. Moin, The structure of the vorticity field in homogeneous turbulent flows, J. Fluid Mech. 176 (1987) 33–66.

[37] V. Suponitsky, J. Cohen, P. Z. Bar-Yoseph, The generation of streaks and hairpin vortices from a localized vortex disturbance embedded in unbounded uniform shear flow, J. Fluid Mech. 535 (2005) 65–100.

[38] T. Watanabe, J. J. Riley, K. Nagata, K. Matsuda, R. Onishi, Hairpin vortices and highly elongated flow structures in a stably stratified shear layer, J. Fluid Mech. 878 (2019) 37–61.

[39] K. Yamamoto, T. Ishida, T. Watanabe, K. Nagata, Experimental and numerical investigation of compressibility effects on velocity derivative flatness in turbulence, Phys. Fluids 34 (2022) 055101.

[40] M. Birouk, B. Sarh, I. Gökalp, An attempt to realize experimental isotropic turbulence at low Reynolds number, Flow, Turbul. Combust. 70 (2003) 325–348.

[41] S. Ravi, S. J. Peltier, E. L. Petersen, Analysis of the impact of impeller geometry on the turbulent statistics inside a fan-stirred, cylindrical flame speed vessel using PIV, Exp. Fluids 54 (2013) 1424.

[42] R. Zimmermann, H. Xu, Y. Gasteuil, M. Bourgoin, R. Volk, J. Pinton, E. Bodenschatz, The Lagrangian exploration module: An apparatus for the study of statistically homogeneous and isotropic turbulence, Rev. Sci. Instrum. 81 (2010) 055112.

[43] S. Xu, S. Huang, R. Huang, W. Wei, X. Cheng, Y. Ma, Y. Zhang, Estimation of turbulence characteristics from PIV in a high-pressure fan-stirred constant volume combustion chamber, Appl. Therm. Eng. 110 (2017) 346–355.

[44] D. Bradley, M. Lawes, M. E. Morsy, Measurement of turbulence characteristics in a large scale fan-stirred spherical vessel, J. Turbul. 20 (2019) 195–213.

[45] R. Theunissen, Adaptive image interrogation for PIV: Application to compressible flows and interfaces, Ph.D. thesis, TU Delft, Delft University of Technology (2010).

[46] J. Westerweel, F. Scarano, Universal outlier detection for PIV data, Exp. Fluids 39 (2005) 1096–1100.

[47] S. B. Pope, Turbulent Flows, Cambridge Univ. Pr., 2000.

[48] D. Xu, J. Chen, Accurate estimate of turbulent dissipation rate using PIV data, Exp. Therm. Fluid Sci. 44 (2013) 662–672.

[49] J. Eisma, J. Westerweel, G. Ooms, G. E. Elsinga, Interfaces and internal layers in a turbulent boundary layer, Phys. Fluids 27 (2015) 055103.

[50] T. Watanabe, K. Nagata, The response of small-scale shear layers to perturbations in turbulence, J. Fluid Mech. 963 (2023) A31.

[51] F. G. Jacobitz, K. Schneider, Scale-dependent analysis of the return to isotropy from anisotropic homogeneous turbulent shear flows originating from Batchelor and Saffman turbulence, Int. J. Heat Fluid Flow 116 (2025) 109927.

[52] T. Mori, T. Watanabe, K. Nagata, Nearly homogeneous and isotropic turbulence generated by the interaction of supersonic jets, Exp. Fluids 65 (2024) 47.

[53] A. N. Kolmogorov, Dissipation of energy in the locally isotropic turbulence, Proc. Roy. Soc. A 434 (1991) 15–17.

[54] S. G. Saddoughi, S. V. Veeravalli, Local isotropy in turbulent boundary layers at high Reynolds number, J. Fluid Mech. 268 (1994) 333–372.

[55] I. Stiperski, G. G. Katul, M. Calaf, Universal return to isotropy of inhomogeneous atmospheric boundary layer turbulence, Phys. Rev. Lett. 126 (2021) 194501.

[56] T. Watanabe, Efficient enhancement of turbulent entrainment by small-scale shear instability, J. Fluid Mech. 988 (2024) A20.

[57] M. Hayashi, T. Watanabe, K. Nagata, The relation between shearing motions and the turbulent/non-turbulent interface in a turbulent planar jet, Phys. Fluids 33 (2021) 055126.